JOURNAL OF PROPULSION AND POWER
Vol. 24, No. 3, May–June 2008

Experimental Studies of Pylon-Aided Fuel Injection into a Supersonic Crossflow

Mark R. Gruber[*] and Campbell D. Carter[*]
U.S. Air Force Research Laboratory,
Wright–Patterson Air Force Base, Ohio 45433
Daniel R. Montes,[†] Lane C. Haubelt,[‡] and Paul I. King[§]
Air Force Institute of Technology,
Wright–Patterson Air Force Base, Ohio 45433
and
Kuang-Yu Hsu[¶]
Innovative Scientific Solutions, Inc., Dayton, Ohio 45440

DOI: 10.2514/1.32231

An investigation of the nonreacting flow associated with pylon-aided gaseous fuel injection into a Mach 2 crossflow is described. In this study, a small pylon was positioned just upstream of a circular flush-wall fuel injector. Three pylon geometries were studied, along with a no-pylon reference case. In all cases, a typical cavity-based flameholder was positioned downstream of the fuel injector. The injectant plume characteristics were interrogated using a variety of laser-based and probe-based measurement techniques. Planar laser-induced fluorescence of nitric oxide was used to study the instantaneous plume structure. Spontaneous vibrational Raman scattering provided time-averaged plume characteristics and mixing information. Probe-based instrumentation was used in conjunction with the mixing data to estimate the total pressure losses associated with each configuration. Each pylon had a unique influence on the fuel-injection plume. In all cases, the presence of the pylon resulted in improved fuel penetration into the supersonic crossflow without significantly changing the total-pressure-loss characteristics. Mixing efficiencies of the pylon-aided injection cases were not substantially different from the reference case.

Nomenclature

A_f = flammable plume area
A_i = injection-port area
A_p = plume area
d = injector diameter
h = pylon base height
L = pylon length
P_{oj} = jet stagnation pressure
P_t = local total pressure
$\bar{P}_t$ = mass-averaged total pressure
$P_{t,\mathrm{ref}}$ = reference total pressure
$\bar{q}$ = jet-to-freestream momentum-flux ratio
T_{oj} = jet stagnation temperature
u = local velocity
w = pylon base width
Xp = distance between the pylon trailing edge and the injector centerline
x = streamwise position
x_{flam} = distance to reach the upper flammability limit
x_{fm} = fully mixed distance
y = transverse position
y_c = center of mass penetration
y_p = plume penetration
z = spanwise position
Δz = plume lateral spread
θ = pylon wedge angle
ρ = local density
ϕ = local equivalence ratio
$\phi_{\max}$ = maximum local equivalence ratio
ω = total-pressure-loss coefficient

I. Introduction

EFFICIENT fuel injection and mixing are critical to the successful development of a hypersonic airbreathing propulsion system. Supersonic velocities within the combustor section significantly limit the time available for mixing and combustion, especially when using hydrocarbon fuels. Various fuel-injection techniques, from different arrangements and shapes of flush-wall injectors to in-stream injection concepts (e.g., ramps, struts, etc.), have been explored in an attempt to enhance the fuel–air mixing rate [1–10]. In general, the larger the disruption a fuel injector generates in the supersonic flow, the more effective the mixing of fuel and air. However, disruptions to the supersonic flow also impose penalties associated with stagnation pressure loss and possibly material heating effects (as in the case of an in-stream injector). Ultimately, the benefits of mixing enhancement must be compared with the associated detriments of pressure loss in any candidate fuel-injection scheme.

Pylon-aided fuel injection has been investigated as a method for introducing liquid or gaseous fuel into the supersonic airstream in the inlet duct well upstream of the combustor [11–13]. In this approach, a small aerodynamically shaped fin (called a pylon) is positioned just upstream of a fuel injector. The pylon temporarily shields the fuel jet from the supersonic approach flow, thereby delaying the fuel–air interaction. In this preinjection scheme, the fuel would have a substantially longer time to atomize, vaporize, and mix with the airstream before entering the combustion region. An important consideration for this approach to be successful is the prevention of

---

Received 18 May 2007; revision received 9 November 2007; accepted for publication 18 November 2007.

[*] Senior Aerospace Engineer. Associate Fellow AIAA.

[†] 1st Lieutenant, U.S. Air Force; currently, Aerospace Engineer, Eglin Air Force Base, FL 32542.

[‡] Captain, U.S. Air Force; currently, Aircraft Performance Engineer, 416th Flight Test Squadron, Edwards Air Force Base, CA 93524.

[§] Professor, Department of Aeronautics and Astronautics. Senior Member AIAA.

[¶] Senior Research Scientist. Senior Member AIAA.

premature reaction. If a flammable mixture of fuel and air resides in the boundary layer, it is possible that combustion could occur well upstream of the combustor, resulting in potentially catastrophic consequences. Results from these studies [11–13] suggested that pylon-aided fuel injection could enhance the fuel jet penetration into the supersonic flow, compared with simple wall injection without a pylon. Results also suggested that little, if any, fuel remained in the near-wall region. This is in stark contrast to traditional normal flush-wall injection without a pylon, in which some fuel always remains near the wall. Vinogradov et al. [14] provided a review of various efforts using pylon-aided fuel injection conducted at the Central Institute of Aviation Motors and the University of Florida.

Recently, Gilinsky et al. [15,16] and Akyurtlu et al. [17] initiated experimental and computational studies using a supersonic inlet fitted with a series of pylons. Initial results from these investigations suggest that the pylons can enhance mixing before the fuel–air mixture reaches the combustor and that the pylons may improve certain aspects of inlet performance.

The focus of the current work was on experimentally studying the influence of three different pylon geometries positioned upstream of a simple flush-wall gaseous fuel injector. In this effort, the pylon-aided injector was examined in the context of a typical hydrocarbon-fueled combustor flowpath that included a cavity-based flameholder. In this way, examinations of the interaction between the flameholder and the injector were possible [18,19]. Nonintrusive and probe-based measurement techniques were used to investigate the instantaneous and time-averaged characteristics of the fuel plume, the fuel–air mixing process, and the pressure losses associated with the pylon-injector flowfield. These results were also compared directly with similar data obtained from a reference injection case without a pylon.

II. Experimental Resources

A. Research Laboratory

The facility used in this investigation was designed to allow basic studies of supersonic flows using conventional and nonintrusive diagnostic techniques. A continuous supply of clean compressed air is available to provide stagnation conditions up to 922 K and 2.8 MPa and a total maximum flow rate of 13.6 kg/s. A backpressure control valve positioned in the facility exhaust section allows remote control of the backpressure in the test section. Additional details describing the facility and its capabilities may be found elsewhere [20].

A two-dimensional converging–diverging Mach 2 nozzle section configured with an asymmetric nozzle was used to develop the desired inlet conditions. The test section was connected directly to the 50.8-mm-high by 152.4-mm-wide exit of the nozzle. The test section had a constant-area section (177.8 mm long), followed by a divergent combustor (2.5 deg over a 740-mm length). A modular cavity was flush-mounted in the divergent combustor. The cavity was recessed from the surface with a 90-deg rearward-facing step, and the trailing edge was configured with a 22.5-deg ramp. The current flameholder configuration had a depth of 16.5 mm and a length of 66 mm (from the point of separation to the ramp midpoint). Optical access to the test section was available through three fused silica windows mounted in either side wall and the top wall.

B. Pylon-Injector Geometries

Four injection schemes were used in this investigation. The reference case was a simple circular transverse injection port ($d = 1.59$ mm). Each of the three pylon-injection cases used the same injector port. A schematic of a representative pylon geometry is shown in Fig. 1; the details of each of the three configurations employed in this study are provided in Table 1. These pylons were designed based on earlier results [11–13]. Figure 2 contains a schematic of a typical pylon-injector configuration as installed into the flowpath. Table 2 contains the operating conditions for the various experiments conducted in this investigation. In all cases, the jet was sonic and the supersonic crossflow was characterized by a Mach number of 1.98, stagnation pressure of 345 kPa, and stagnation temperature of 296 K. Two axial locations were available for inserting the pylon/injector combination, as shown in Fig. 2. Both positions were used in this study. The upstream position was used in conjunction with the planar imaging measurements, and the Raman-scattering and probe-based measurements were made with the pylon in the downstream position.

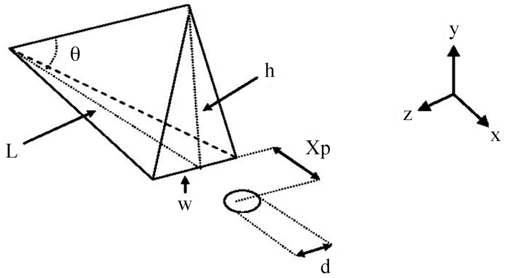

Fig. 1 Pylon and injection-port geometry.

C. Measurement Techniques

1. Nitric-Oxide Planar Laser-Induced Fluorescence

Instantaneous measurements of the mixing flowfield were obtained using planar laser-induced fluorescence (LIF) of nitric oxide. In the planar laser-induced fluorescence of nitric oxide (NO-PLIF) technique, the injectant is composed of a mixture of air (greater than 95% by volume) and NO-doped N_2; the air and N_2 are mixed upstream of the injection point (so that conversion to NO_2 is minimal) and the final NO mole fraction is less than 500 ppm (volume basis). A Lumonics Hyperdye dye laser was pumped with the second harmonic of an injection-seeded Spectra-Physics Nd:YAG laser (GCR-170). The dye-laser output was frequency-doubled using an Inrad Autotraker III. Within a second Autotraker III, the doubled-dye beam was frequency-mixed with the residual IR beam from the Nd:YAG. The dye laser was set to a wavelength of 574 nm to produce frequency-mixed radiation at 226 nm to couple to the $R_1(6)$ transition of the $A^2\Sigma^+ - X^2\Pi$ (0, 0) band; the $N_1 = 6$ ground state was selected to minimize the Boltzmann fraction variation (associated with total temperatures ~290 K). A portion of the 226-nm beam was split off and directed over a small burner. The resulting NO-laser-induced fluorescence was measured with a photomultiplier tube and was continuously monitored on an oscilloscope to ensure good overlap with the desired molecular transition; this allowed the dye-laser tuning to be periodically optimized during the course of the experiments. The LIF images were not corrected for variations in line broadening, electronic quenching, or ground state population. Because the injectant is predominantly composed of air, there is no significant difference in the electronic quenching rate, due to changes in gas composition as the injectant mixes with the tunnel air; furthermore, in the absence of collisional line broadening, an increase in the local static pressure, for example, will increase both the electronic quenching rate and the NO number density, leaving the LIF signal unchanged. However, an increase in local pressure will decrease the LIF signal through a reduction in the laser-transition coupling, the extent of which is determined by the laser spectral line width and the magnitude of increase in the transition line width. Nonetheless, a decrease in signal intensity can be taken to indicate a

Table 1 Pylon geometries

	Medium pylon	Tall pylon	Wide pylon
Height h, mm	6.35	9.52	6.35
Length L, mm	10.92	16.51	10.92
Width w, mm	1.78	1.78	2.54
Injector spacing X_p, mm	3.56	3.56	5.08
Wedge angle θ, deg	30.2	30.0	30.2
h/d	4	6	4
w/d	1.12	1.12	1.60
X_p/d	2.24	2.24	3.20

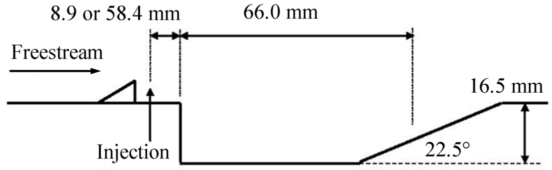

Fig. 2 Flowpath schematic.

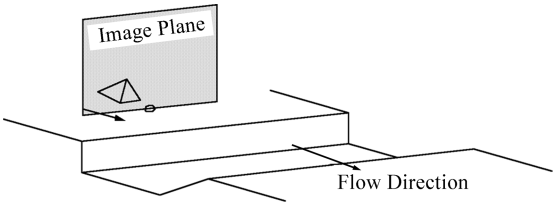

Fig. 3 Schematic illustrating the fluorescence image-plane orientation.

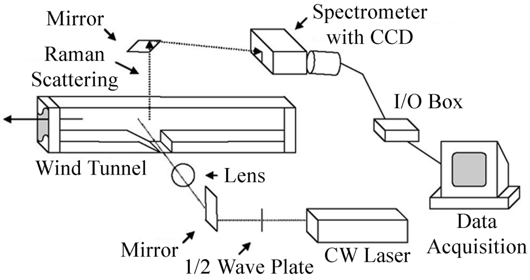

Fig. 4 Raman-scattering schematic.

decrease in NO concentration and is therefore representative of mixing and dilution of the jet plume with the freestream air. This interpretation is better in the far field of injection, in which temperature and pressure variations are more modest.

The laser sheet was formed using a pair of lenses: a planoconcave cylindrical lens (-50-mm focal length) and a planoconvex spherical lens (1000-mm focal length). This arrangement resulted in a sheet height and thickness of about 75 mm and $\sim 300\ \mu\text{m}$, respectively. This sheet was directed across the span of the test section (through the fused silica windows), and the resulting fluorescence was imaged off-axis (to the sheet normal) using a Princeton Instruments Superblue PIMAX intensified CCD camera with a 512 × 512 pixel array. In this arrangement, cross-sectional views (y–z planes) of the injectant plume were captured (see Fig. 3). The camera pixels were binned 2 × 2 before readout so that the camera could achieve a 10 frame/s readout, thus matching the laser repetition rate. Also, the camera gate was set to 100 ns, but the fluorescence pulse is only slightly longer than the laser pulse; the interrogation time is thus about 10 ns. The camera was fitted with a 105-mm focal length, $f4.5$ Nikon UV lens. A Schott UG-5 filter blocked scattering at 226 nm [as well as fluorescence from the (0, 0) band] and transmitted fluorescence from the (0,1), (0,2), and (0,3) bands, respectively, at 236, 246, and 257 nm, respectively. A Scheimpflug-mount mitigated-image blur is associated with off-axis image collection. The transmitting and receiving optics were positioned on a traversing table, allowing remote positioning of the measurement volume at any desired station in the flowfield. Axial positions corresponding to $x/d = 0$, 4, 8, 12, 16, 20, 24, and 32 were interrogated, where $x/d = 0$ corresponds to the center of the injector.

Ensembles of end-view images were captured for all cases listed in Table 2. Each ensemble consisted of 200 instantaneous images. These were supplemented with images collected in the absence of fuel injection (for background subtraction) and so-called flat-field images (for correcting laser sheet and imaging nonuniformities). The flat-field images were obtained by filling the tunnel, under no-flow conditions, with a small amount of NO-laden air. NO-PLIF images were then acquired at all axial probing locations. Before postprocessing, images were also corrected for perspective distortion using a reference image of a dot card having known interdot spacing. A set of coordinates for four corner dots was input into a MATLAB code employing the projective algorithm; the dewarped dot-card image was then inspected to ensure that it reasonably matched the undistorted dot card. This transform was then applied to all warped images. Note that all other image calculations were performed with the ImageJ processing package .[**]

Table 2 Injectant operating conditions

Case	Pylon	P_{oj}, kPa	T_{oj}, K	q	Measurement technique
1	——	345	291	1	NO-PLIF, Raman, probe
2	——	689	292	2	NO-PLIF
3	——	1379	293	4	NO-PLIF, Raman, probe
4	Medium	345	290	1	NO-PLIF, Raman, probe
5	Medium	689	292	2	NO-PLIF
6	Medium	1379	292	4	NO-PLIF, Raman, probe
7	Tall	345	289	1	NO-PLIF, Raman, probe
8	Tall	689	289	2	NO-PLIF
9	Tall	1379	289	4	NO-PLIF, Raman, probe
10	Wide	345	288	1	NO-PLIF, Raman, probe
11	Wide	689	288	2	NO-PLIF
12	Wide	1379	289	4	NO-PLIF, Raman, probe

2. *Raman Spectroscopy*

Time-averaged measurements of the mixing flowfield were obtained using spontaneous vibrational Raman scattering [21,22]. A schematic of the Raman spectroscopy setup used in the experiment is shown in Fig. 4. In these experiments, ethylene was injected into the supersonic air crossflow. The excitation source was provided by a Spectra-Physics Millenia Pro continuous-wave (CW) Nd:YVO laser producing 8.5 W at 532 nm. This laser line was focused using a 500-mm focal-length lens and transmitted into the flowfield through one of the side-wall windows along the z axis. The scattered light was collected and focused with a Nikon 35-mm camera lens through the test section's top window. A Schott OG-590 filter was placed before the lens to suppress laser scattering. The light was dispersed using a Kaiser Holospec $f1.8$ imaging spectrometer and detected using an Andor backilluminated, thermoelectrically cooled, spectroscopy CCD camera (binned pixel width of $50\ \mu\text{m}$). A mechanical shutter (Uniblitz) was used to control the camera exposure. The spectrometer grating permitted both nitrogen and ethylene spectra (at 607 and 634 nm, respectively) to be acquired. The nitrogen signal was relatively narrow (1 to 2 binned pixel widths) and the ethylene signal was relatively broad (10 to 20 binned pixel widths). The spectral resolution was limited by the focus of the scattering onto the spectrometer entrance slit (rather than by the entrance slit width), and the imaged length of the probe was determined by the slit height and was ~ 30 mm long. The optics were mounted on a traversing table, allowing movement in the transverse y and streamwise x directions.

Image acquisition was synchronized with traversing-table movements so that data collection was automated. Once steady-state operating conditions were established in the test section, the measurement volume was placed at its initial position and data were collected for 20 s (leaving the shutter open for this time). Following the data transfer from the camera to the computer, the traversing table moved to its next preprogrammed position and the process repeated. Once the fuel plume had been completely traversed (i.e., images showed no ethylene signal), the fuel was turned off. The probe volume was then returned to its initial position. This process was repeated to obtain 29 measurement-volume locations for a given axial station.

An extensive data-reduction process was used to determine ethylene and nitrogen number densities from the collected

---

[**] Data available online at http://rsb.info.nih.gov/ij/ [retrieved 17 March 2008].

Raman-scattering images. Calibration of the raw-signal counts (conversion to number density in molecules/cm^3) was accomplished with the following procedure:

1) Using air only in the tunnel (under known ambient temperature and pressure conditions), the nitrogen Raman-scattering signal was measured (thus providing the nitrogen calibration).

2) The tunnel was sealed off on either end, with foam so that the tunnel pressure remained at ambient conditions (confirmed by measurement); ethylene was injected into the tunnel and allowed to mix thoroughly. A second Raman-scattering measurement was made; the reduction in the nitrogen signal (from the first measurement) allowed determination of the ethylene number density from the ideal gas law (because tunnel pressure and temperature were known) and thus the Raman-scattering calibration factor. The bias error in calibration of the signals is estimated to be ±4% so that the bias equals ±4% of the measured value.

These data were further reduced to values of the fuel–air equivalence ratio assuming that differential diffusion of nitrogen and oxygen is not present (i.e., the molar ratio of nitrogen to oxygen in air is 3.76). Further details of the data-reduction process are provided elsewhere [23].

An error analysis was completed for the Raman-scattering results [23]. The two significant sources of error were identified to be systematic error in the optical calibration constants and precision error from variations in individual measurements. These errors were combined using a root-sum-square approach to yield an overall uncertainty on species number density and ϕ. Using this approach, the uncertainty in ϕ was found to be 3.8% of the local value.

3. *In-Stream Probing*

Three conventional probes were used to examine the flowfield at an axial location of $x/d = 12$. Measurements were performed using Pitot and cone-static pressure probes and a total temperature probe. The probes were inserted through a movable side wall of the test section. They were secured within identical diamond-wedge struts. A two-axis computer-controlled traversing mechanism allowed the probes to be positioned in the spatial region bounded by $-8 < z/d < 8$ and $0 < y/d < 9$. These data were used in conjunction with the Raman-scattering data and a computerized solution algorithm developed by Fuller et al. [5] to determine the time-averaged aerothermodynamic properties of the flowfield. Fuller et al. also conducted an uncertainty analysis for the probe-based measurements; the results of this analysis are reproduced here: the uncertainties in stagnation pressure, Mach number, density, static pressure, static temperature, and velocity were determined to be 2.8, 1.7, 3.0, 2.8, 0.8, and 1.3% of the local values, respectively. These results were used to estimate the error in the total-pressure-loss coefficient as 4.3%.

III. Results and Discussion

Various results obtained in this investigation will be presented in the following sections. Planar imaging results will be described first. These will be followed by the results obtained from the Raman-scattering and probe-based measurements.

A. NO-PLIF Imaging Results

1. *Instantaneous Images*

Figure 5 contains representative instantaneous NO-PLIF end-view images obtained from the four injection configurations. In each image, the injection pressure and image plane correspond to $\bar{q} = 4$ and $x/d = 16$. Injection is from the lower boundary of each image at the spanwise centerline ($y/d = 0$ and $z/d = 0$). Light regions indicate the presence of nitric oxide and dark regions indicate pure freestream fluid. These images reveal the complex nature of the injectant/crossflow interaction, especially at the interface between jet and freestream fluids. The highly convoluted interface between these fluids contains a variety of large- and small-scale structures that are principally responsible for fuel–air mixing.

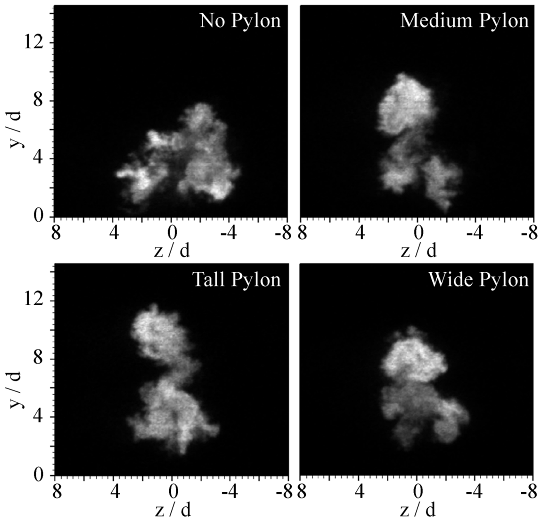

Fig. 5 Instantaneous NO-PLIF end-view images ($x/d = 16$).

2. *Ensemble-Averaged and Standard-Deviation Images*

Figures 6–9 show the mean and standard-deviation images at $\bar{q} = 4$ for all four injection configurations at image-plane locations corresponding to $x/d = 0$, 16, and 32 (using a linear grayscale). The intensity values for the statistical images correspond to the LIF signal level (or the standard deviation of the signal level) relative to that in the corresponding ensemble-averaged flat-field images.

When no pylon is installed (Fig. 6), the jet plume exhibits the familiar behavior observed in previous research [24,25]. At the jet injection location ($x/d = 0$), the plume is mostly concentrated near the floor. The standard deviation at this location shows a large jet-freestream interaction over the top of the plume. The fluid then quickly develops into a lifted formation with a pair of counter-rotating vortices ($x/d = 16$). The mean images show that most of the

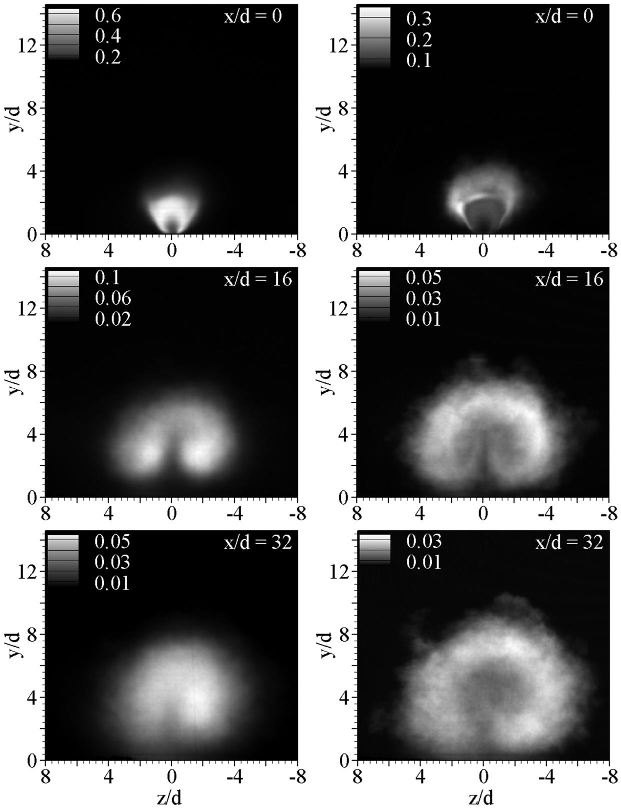

Fig. 6 Ensemble-averaged (left) and standard-deviation (right) images for case 3.

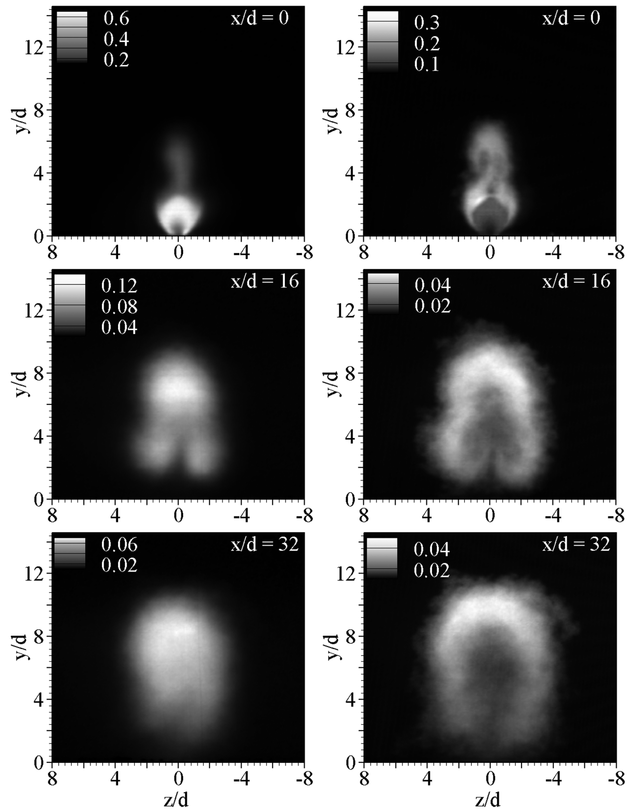

Fig. 7 Ensemble-averaged (left) and standard-deviation (right) images for case 6.

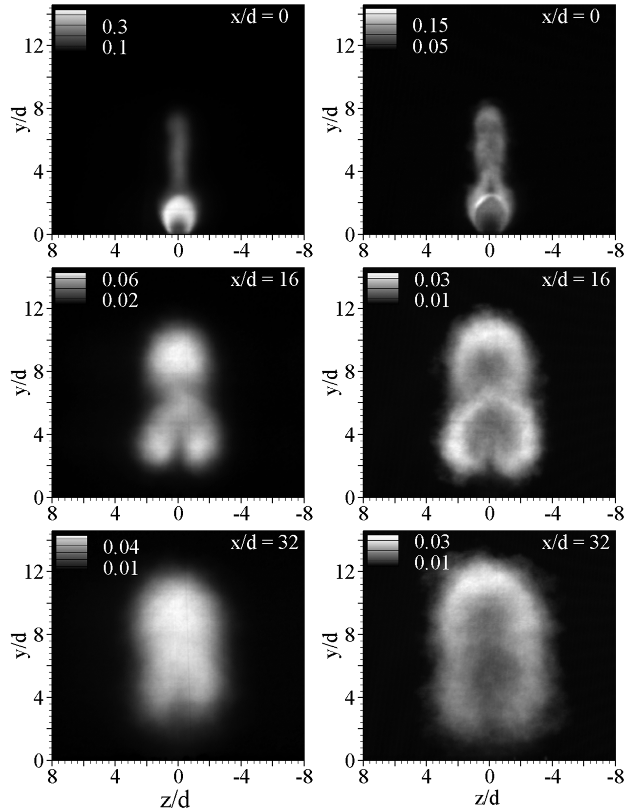

Fig. 8 Ensemble-averaged (left) and standard-deviation (right) images for case 9.

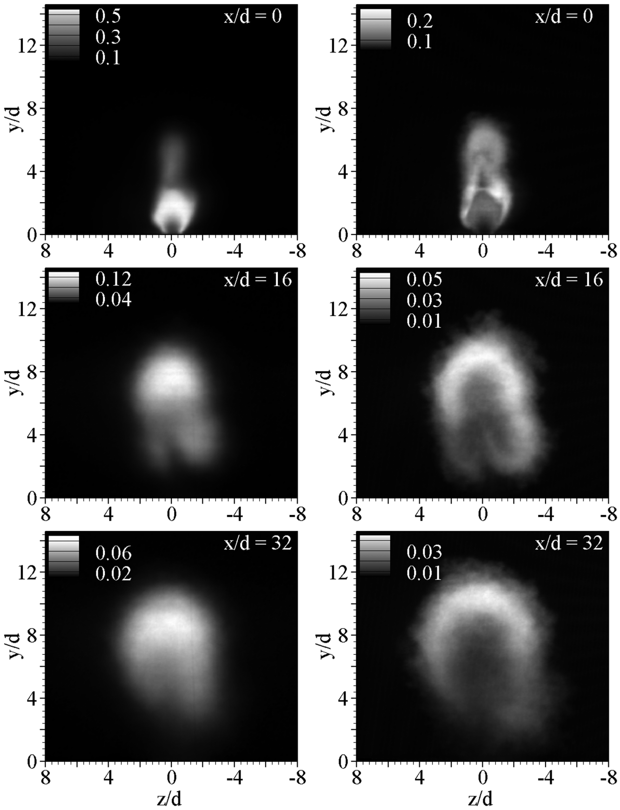

Fig. 9 Ensemble-averaged (left) and standard-deviation (right) images for case 12.

jet fluid is concentrated in these areas, and the standard deviation illustrates the strong interaction around the side and bottom of the plume. At the downstream locations, the peak intensities within the standard-deviation images are comparable with those in the average images, indicating strong shot-to-shot variations in the plume shape (as observed in Fig. 5). These areas of strong interaction (bright white on the standard-deviation images) are large and well-defined. Some jet fluid remains near the floor; this could result in fuel being deposited in the boundary layer.

When injection occurs behind the medium pylon (Fig. 7), the jet plume remains largely near the floor, but with a small amount of NO penetrating farther into the freestream (above the pylon). The jet then immediately widens to a thickness greater than the pylon, with a high-interaction zone in the base area. By the $x/d = 16$ location, jet fluid has penetrated farther into the crossflow. The familiar counter-rotating formations are evident but appear to play less of a role, because the standard deviation shows the interaction zone shifting up to match the lift in jet concentration. By $x/d = 32$, the majority of the jet fluid and interaction is in the upper area, which has become wider and more pronounced. This three-part process (immediate penetration and widening, transfer of fluid concentration away from the floor and counter-rotating areas, and settling of the fluid in the now-wide upper area) is observable in all pylon configurations. The process suggests that the general role of the pylons is to lift fuel from the floor and disperse it higher into the crossflow, lessening the vortex generation while maintaining a large interaction zone. All pylons increase the penetration height and reduce the amount of fuel located near the floor, compared with the reference case. Images from cases operated at reduced $\bar{q}$ (not shown) reveal similar features [18,26].

Injection behind the tall pylon (Fig. 8) shows immediate penetration above the main plume, and the standard deviation shows a high initial level of development in the upper area. At $x/d = 16$, the jet fluid appears to be approximately equally split between the upper and lower areas. Here, the plume shape distinctly suggests two independent regions. The counter-rotating structures begin to diffuse farther downstream and, as in the medium-pylon case, more fluid is concentrated in the upper area. The tall-pylon case shows much higher penetration into the freestream than either the reference or the medium-pylon cases. The tall pylon also results in the fuel being lifted relatively high off the floor.

Injection behind the wide pylon (Fig. 9) exhibits many characteristics established by the other pylons. Unlike the other pylon cases, the plume generated in this case appears skewed or asymmetric. It is believed that the pylon itself may be slightly misaligned with respect to the crossflow (e.g., situated at a slight angle of attack). What sets the wide-pylon case apart from those shown in previous images is the rapidness of jet penetration and initial upper-area development. Upon injection, the jet fluid and interaction zone quickly penetrate to a height significantly higher than the pylon height, and by $x/d = 8$ (not shown), the transition from the lower to the upper area begins. The jet quickly lifts off the floor. All injection pressures show the jet quickly transitioning and lifting from the floor, followed by a slow transition to the final plume shape. This may be advantageous, because the pylon quickly deposits fuel into the core flow, allowing it to mix. In fact, local maximum standard-deviation values (normalized by initial maximum intensity, as discussed previously) show the most intense interaction occurring in the wide-pylon case.

The ensemble-averaged images were further analyzed to obtain plume penetration, lateral spread, center of mass penetration, and plume area. In this analysis, the maximum intensity was identified in each of the ensemble-averaged images. The plume boundary was determined by searching the images for intensity values corresponding to 10% of this maximum intensity. The plume penetration y_p was determined from the upper extent of this contour. The lateral spread Δz was determined by finding the widest extent of the contour. The location of the center of mass y_c was determined using the intensity and spatial information contained in the images. Finally, the plume area A_p was calculated by counting the number of pixels within the contour. Figure 10 shows graphical representations of these parameters as functions of axial distance for the $\bar{q} = 4$ injection cases. Table 3 presents these data from all injection cases at $x/d = 20$.

The tall pylon substantially enhances the fuel jet penetration (Fig. 10a). The wide pylon has a slight advantage over the medium pylon, which contradicts the predictions by Gouskov et al. [13] All pylons yield higher penetration than simple wall injection with no upstream pylon. Table 3 indicates the same results at the lower injection pressures. All pylon-injection cases have narrower injectant plumes than those found in a simple wall jet (Fig. 10b). Pylons also improve the penetration of the center of mass of the jet plume for all injection conditions studied. The plume area remains relatively constant for all cases of the same jet-to-freestream momentum-flux ratio.

B. Raman-Scattering Results

1. *Equivalence-Ratio Images*

The Raman-scattering measurements were processed to determine time-averaged values of the ethylene–air equivalence ratio for all of the measurement stations in each injection case (see Table 2). The results for all injection cases are shown in Figs. 11–14. In these plots, the flow direction is out of the paper and the same color scale is used throughout ($0.1 < \phi < 12.7$).

Figure 11 presents the results from injection without a pylon at $\bar{q} = 4$. At $x/d = 7.2$, a pair of counter-rotating vortices is clearly seen as two lobes in the image. Most of the fuel is concentrated within the interior of the vortices and little mixing with the main flow is evident. At $x/d = 12$, the fuel plume begins to increase in area, and fuel concentration within the vortices decreases. As axial distance increases, more fuel becomes entrained in the cavity ($y/d < 0$). At $x/d = 29.6$, the plume is no longer dominated by the vortex structures. At these injection conditions, the counter-rotating vortices are still apparent, but they have lost much of their previous resolution. The plume continues to expand in area and apparent penetration height.

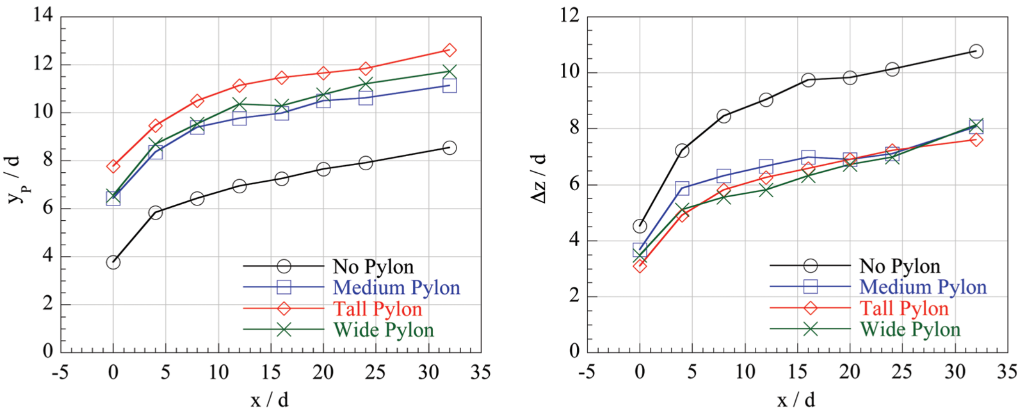

a) Plume penetration

b) Lateral spread

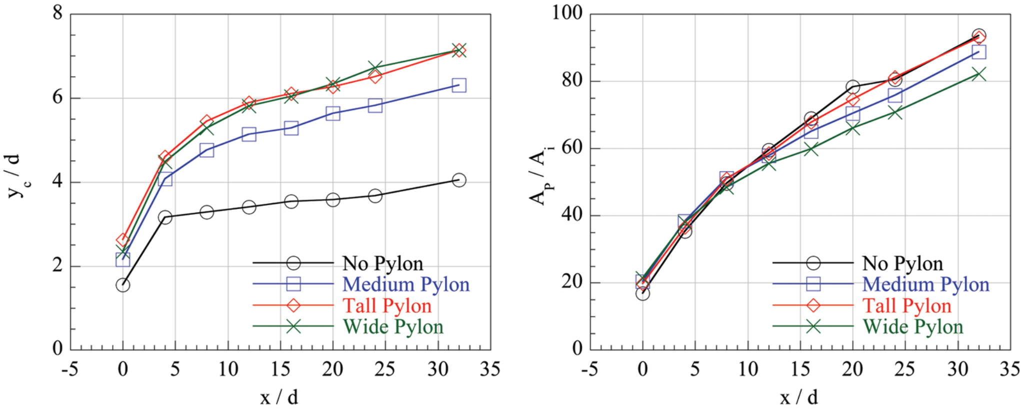

c) Center of mass penetration

d) Plume area

Fig. 10 Ensemble-averaged NO-PLIF image data for all configurations at $\bar{q} = 4$.

Table 3 Ensemble-averaged image data from all cases at $x/d = 20$

	No pylon			Medium pylon			Tall pylon			Wide pylon		
$\bar{q}$	1	2	4	1	2	4	1	2	4	1	2	4
y_p/d	4.94	6.23	7.64	7.32	8.81	10.48	8.23	10.03	11.65	7.65	8.94	10.74
$\Delta z/d$	6.52	7.74	9.81	5.29	5.87	6.90	5.10	5.23	6.90	5.68	6.13	6.71
y_c/d	2.23	2.90	3.58	4.50	5.30	5.63	4.99	5.93	6.26	4.83	5.64	6.33
A_p/A_i	33.4	49.9	78.3	33.4	45.9	70.4	35.1	47.5	74.6	35.2	46.4	66.1

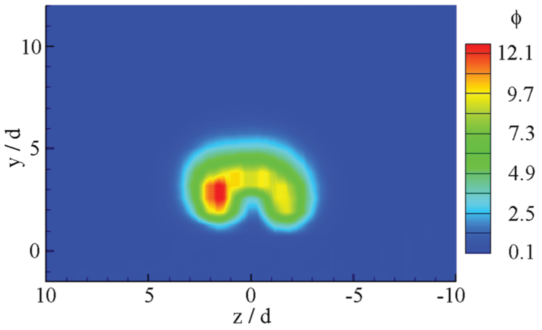

a) x/d = 7.2

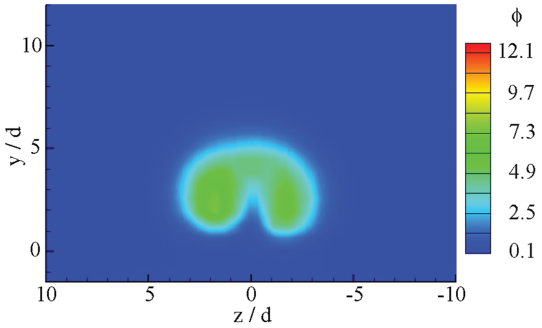

b) x/d = 12.0

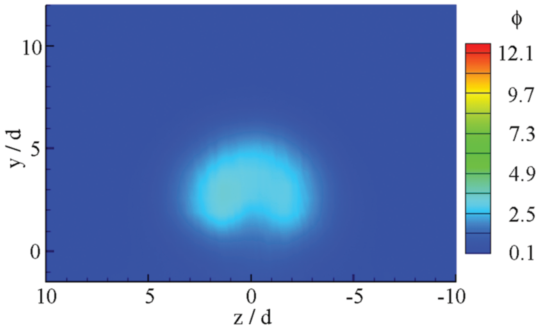

c) x/d = 29.6

Fig. 11 Equivalence-ratio contours for case 3.

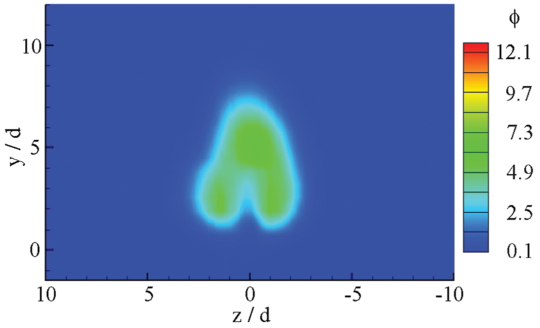

Fig. 12 Equivalence-ratio contours for case 6 ($x/d = 12$).

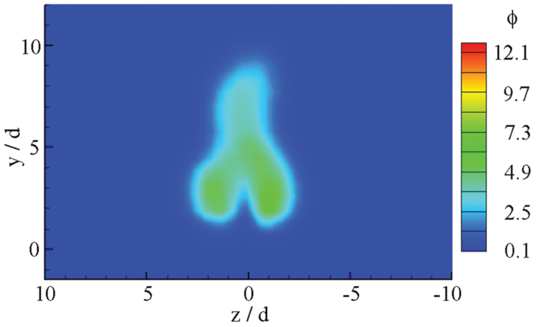

Fig. 13 Equivalence-ratio contours for case 9 ($x/d = 12$).

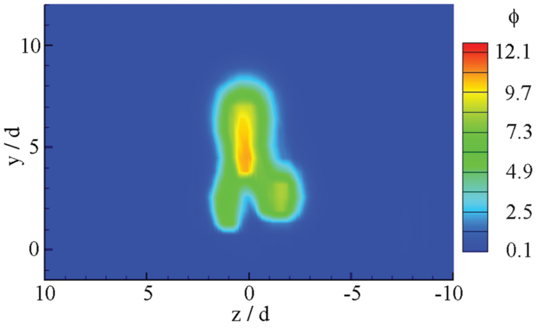

a) x/d = 7.2

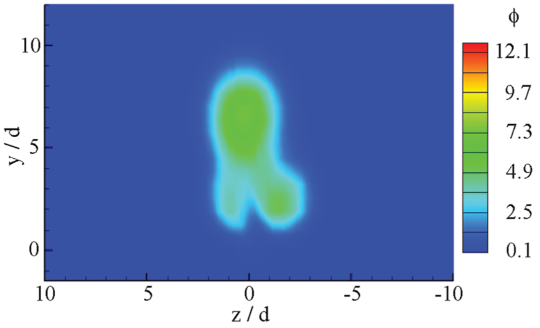

b) x/d = 12.0

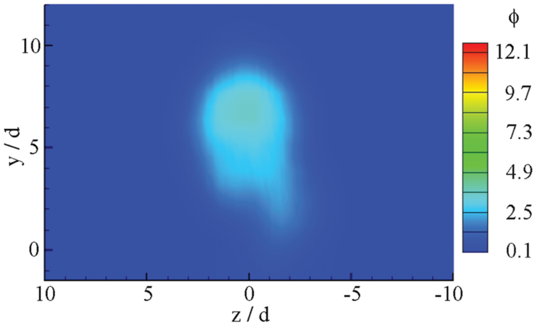

c) x/d = 29.6

Fig. 14 Equivalence-ratio contours for case 12.

Results from the medium-pylon and tall-pylon cases from $x/d = 12.0$ are shown in Figs. 12 and 13, respectively. Injection downstream of the medium pylon results in a plume with features similar to the no-pylon-injection case at the same axial station (i.e., counter-rotating vortex pair), but with greater penetration and narrower spread. In the case of the tall pylon, a substantial increase in penetration is observed, compared with the no-pylon case at $x/d = 12.0$ (Fig. 11b). The plume remains narrower than the case without a pylon, and the counter-rotating vortex pair continues to dominate the plume structure, suggested by the two lobes at the bottom of the plume.

Measured equivalence ratios are presented for the wide pylon at $x/d = 7.2$, 12.0, and 29.6 in Fig. 14. At $x/d = 7.2$, it is apparent that the distribution of fuel is drastically changed, compared with the no-pylon case, due to the presence of the pylon. Penetration is increased and plume width is decreased, compared with the baseline case. Additionally, the maximum equivalence ratio present at this axial station is lower than with the baseline case. A third fuel lobe, as observed in the medium- and tall-pylon-injection cases, is present, and the location of the maximum equivalence ratio is lifted above the vortex pair. Note that the asymmetric distribution of fuel in the vortex pair is the opposite of that observed in the case without a pylon. This suggests that an additional three-dimensional quality is added to the flow by the pylon shape and suggests possible misalignment with the freestream. At $x/d = 12.0$ (Fig. 14b), the major concentration of fuel continues to migrate away from the counter-rotating vortices into the freestream and away from the interior of the plume. By $x/d = 29.6$ (Fig. 14c), the counter-rotating vortex pair is almost totally absent as the plume continues to expand.

2. *Mixing Analysis*

The Raman data were further analyzed to obtain quantitative assessments of various aspects of the plumes, including fuel plume properties (penetration and area) and decay of the maximum equivalence ratio. For this analysis, the $\phi = 0.2$ contour was used to define the plume boundary. Once identified, the upper edge of this contour defined the plume penetration and the area bounded by this contour defined the plume area A_p. An additional area was determined based on the flammability limits of ethylene in air at standard temperature and pressure. The published flammability range covers $0.4 < \phi < 5.5$ [27]; for the purposes of this study, this range was arbitrarily narrowed by 10% in each direction to obtain a more conservative estimate. The upper and lower contours were identified and the area between them (A_f) was determined.

The plume penetration y_p/d is shown for each configuration in Fig. 15. Pylon height is included in the plot as a reference. As expected, the pylons increase plume penetration over the cases without a pylon for both injection pressures. At $\bar{q} = 1$, the plume from the tall-pylon case penetrates the highest over the baseline. As dynamic pressure ratio is increased, plume penetration increases. At $\bar{q} = 4$, the wide and tall configurations have approximately the same increase in plume penetration over the baseline, and the medium configuration has the least increase in plume penetration over the baseline. These results follow the same trends established in NO-PLIF measurements, shown in Fig. 10a. However, the absolute values for plume penetration obtained from the Raman-scattering results are somewhat lower than those found from the NO-PLIF. This result illustrates the benefits of having an absolute measure of concentration to determine plume characteristics. Of the three configurations, the wide pylon results in a greater augmentation in plume penetration as $\bar{q}$ increases, and both the medium and tall pylons produce about the same change.

Figure 16 shows the decay of maximum equivalence ratio with downstream distance for the wide-pylon and reference configurations. Past studies have shown that mixing data vary exponentially in the far-field region, allowing power-law curve fits to be used to predict the rate of change in concentration decay with downstream location [28]. Thus, the current data are fit using power-law expressions. At $\bar{q} = 1$, there is no significant difference in the decay rate of the wide-pylon and reference configurations. At the higher injection pressure ($\bar{q} = 4$), the rate of decay for the wide pylon stays about the same, and the rate for the baseline increases. Note that for the high-$\bar{q}$ case, a transition occurs between the faster near-field mixing associated with the wide pylon and the faster far-field mixing associated with the reference case at $x/d \sim 20$. This is due to the wide pylon's initially lower fuel concentration and the reference case's greater rate of concentration decay. Typically, once the maximum concentration of a fuel reaches stoichiometric conditions, the injectant is considered fully mixed [28]. For this reason, a line is drawn on the figure at stoichiometric conditions. For low-$\bar{q}$ conditions, the distance required for a fully mixed condition (x_{fm}) is approximately $d = 50$ and 60 for the wide-pylon and reference cases, respectively. At the high-$\bar{q}$ condition, x_{fm} increases to about $d = 150$ and 110 for the wide-pylon and reference cases, respectively. These values are comparable with the historical trend of $d = \sim 200$ [28].

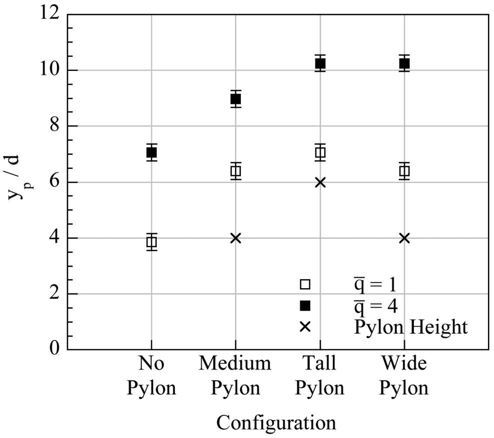

Fig. 15 Plume penetration derived from Raman-scattering measurements ($x/d = 12$).

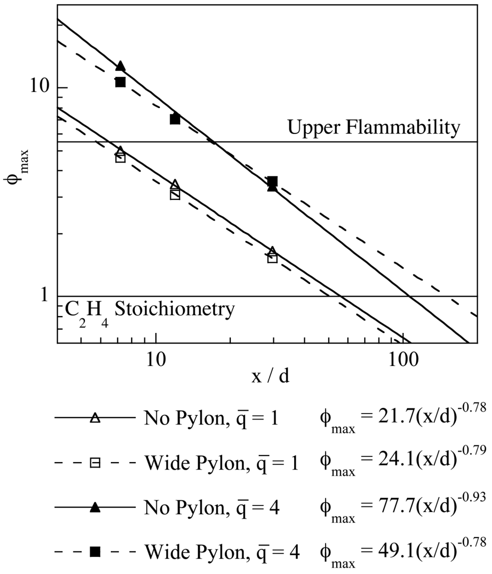

Fig. 16 Concentration decay derived from Raman-scattering measurements.

The accepted practice of declaring an injection flowfield to be fully mixed once the maximum concentration of fuel reaches stoichiometric proportions may not be the best gauge of mixing for combustion (although it does provide data for comparison with previous research). Because most fuels burn at concentrations above stoichiometric, it may be prudent to establish the distance for a plume's maximum concentration to reach the upper flammability limit. This is defined as the flammable mixture distance x_{flam}. At this axial location, the entire plume is at or below the maximum fuel–air ratio required for combustion. A line is included in Fig. 16 to indicate

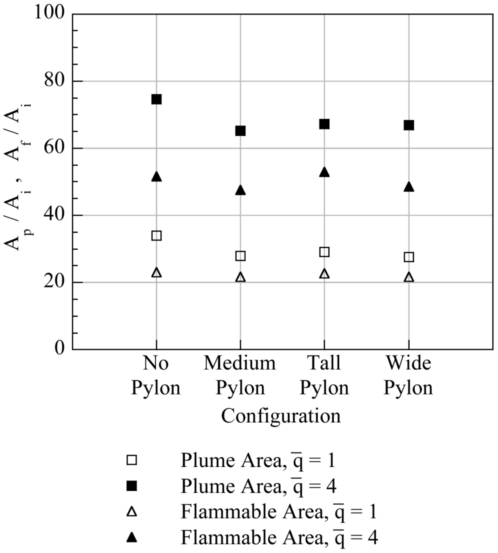

Fig. 17 Plume areas determined from Raman-scattering measurements ($x/d = 12$).

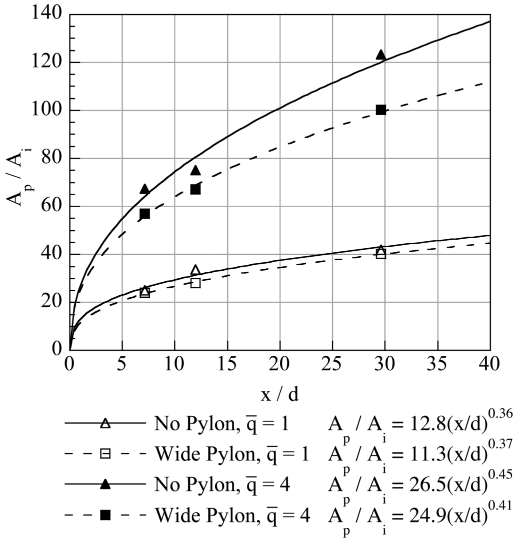

Fig. 18 Variation in plume area with axial position for cases 1, 3, 10, and 12.

the upper flammability limit. At $\bar{q} = 1$, the values of x_{flam} for the baseline and wide configurations shown in Fig. 16 are about $d = 3.5$ and 2.5, respectively. At $\bar{q} = 4$, the values of x_{flam} for the two configurations are almost identical at $d = 18$.

Figure 17 shows the total plume area A_p and flammable plume area A_f normalized by the injection-port area A_i for all test cases at $x/d = 12$. All pylons demonstrate approximately the same total and flammable area at the same injection pressure. An increase in injection pressure causes an increase in both total and flammable plume areas. The reference configuration has a noticeably larger A_p than with the pylons. However, when comparing A_f, the difference between the reference and pylon configurations is not as significant. As a result, the flammable plume areas in the pylon cases are larger fractions of the total plume areas than in the reference case (see Table 4). Both the baseline and tall configurations have slightly larger flammable plume areas than the wide and medium pylons; however, this difference is not substantial enough to deem either configuration to be superior at this streamwise station.

Figures 18 and 19 show the axial variation of A_p and A_f for the reference and wide-pylon configurations. As in previous trajectory plots, a power-law correlation is used to describe the axial variation in area. Plume trajectories for A_p given in Fig. 18 show that for both injection pressures, the reference configuration has increased spreading, compared with the wide pylon over the region studied. At low $\bar{q}$, the reference configuration has a greater plume area, but a spreading rate similar to the wide-pylon case. When $\bar{q}$ is increased to 4, areas and spreading rates are increased in both configurations. At the higher injection pressure, the reference case shows a greater area and spreading rate than with the wide-pylon case. Trajectories of A_f display trends similar to those seen for A_p (see Fig. 19). At both injection pressures, the reference configuration demonstrates larger magnitudes of A_f at each axial location and larger spreading rates than with the wide-pylon configuration. It is also interesting to note that for both low-$\bar{q}$ configurations, the rate of spreading of A_f appears to be less than that of A_p, perhaps indicating that most of the plume is spreading in concentrations outside of the flammability limits. The opposite appears to be evident in the high-$\bar{q}$ cases: the spreading rates of the flammable plume area are greater than the spreading rates of the total plume area, indicating that the plume's fuel is mixing into concentrations within the upper flammable limit faster than in the total plume is spreading. Overall, the reference configuration displays better total and flammable plume spreading than the wide-pylon configuration at both injection pressures. This may be due in part to the reference case's fuel plume being located within the vortex pair, which aids in mixing and spreading. As injection pressure increases, the magnitude and rate of spreading of A_p and A_f increase, indicating that increasing $\bar{q}$ has a favorable effect on plume spreading.

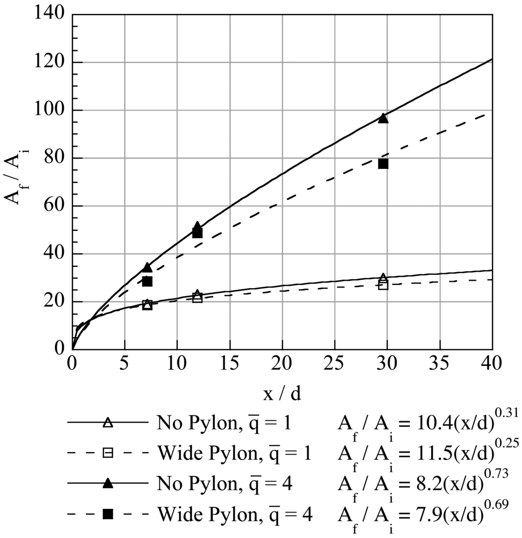

Fig. 19 Variation in flammable plume area with axial position for cases 1, 3, 10, and 12.

Table 4 Ensemble-averaged image data from all cases at $x/d = 20$

Configuration	A_p/A_i, $\bar{q} = 4$	A_f/A_i, $\bar{q} = 4$	A_f/A_p, $\bar{q} = 4$	A_p/A_i, $\bar{q} = 1$	A_f/A_i, $\bar{q} = 1$	A_f/A_p, $\bar{q} = 1$
No pylon	74.6	51.6	0.69	34.0	23.0	0.68
Medium pylon	65.2	47.6	0.73	28.0	21.7	0.77
Tall pylon	67.2	52.9	0.79	29.1	22.7	0.78
Wide pylon	66.9	48.6	0.73	27.7	21.6	0.78

C. In-Stream Probing Results

The probe data analysis routine computed values for the major aerothermodynamic properties of the flow based on the measured pitot pressure, cone-static pressure, total temperature, and species information (determined from the Raman-scattering results). These properties were then used to compute the total-pressure-loss coefficient ω. This property represents a mass-averaged value of total pressure loss for a given region of interest in the flowfield and is determined using Eq. (1).

$$\omega = 1 - \frac{\bar{P}_t}{P_{t,\mathrm{ref}}} \tag{1}$$

In this expression, $\bar{P}_t$ is the mass-averaged total pressure for the region of interest and $P_{t,\mathrm{ref}}$ is the measured tunnel-plenum pressure. Values for $\bar{P}_t$ are determined using Eq. (2).

$$\bar{P}_t = \frac{\int P_t \rho u \mathrm{d}A}{\int \rho u \mathrm{d}A} \tag{2}$$

This definition allows the local impact of flow momentum through an area. A value of $\omega = 1$ means complete total pressure loss and a value of $\omega = 0$ denotes no total pressure loss. Therefore, a small value for ω is desired. It should be emphasized that these values are based on properties from within a given region of interest and are not representative of the total pressure loss associated with the entire flowfield cross section. A consistent cross section was used for all configurations. The cross section spans from $-8 < z/d < 8$ and encompasses a region in the transverse direction that avoids the effect of the bow shock to ensure that the entire plume is captured. Figure 20 gives values of ω for each injector configuration at $x/d = 12$. In the low-injection-pressure cases, ω remains consistent across the injector configurations. All pylons have slightly increased total pressure loss, compared with the reference case at $\bar{q} = 1$. The largest increase at this injection pressure occurs in the tall and wide-pylon configurations, because these pylons have larger cross-sectional areas than in the medium-pylon and reference cases. As $\bar{q}$ is increased to 4, the pressure losses increase. This is to be expected, given the increased plume penetration, area, and the stronger bow shock present in these cases. The tall and wide pylons show little change compared with the reference case: only the medium pylon shows a noticeable decrease in pressure loss compared with the reference configuration. Overall, all configurations have similar total pressure losses for a given injection pressure.

IV. Conclusions

Three pylon-based fuel injectors were experimentally investigated and compared with a reference injection case. All injectors were issued into a Mach 2 crossflow. For each configuration, a range of jet-to-freestream momentum-flux ratios was examined. Planar laser-induced fluorescence of nitric oxide (NO-PLIF) provided instantaneous images of the injectant plume. Ensemble-averaged images were used to determine properties of the fuel plume, including penetration, lateral spread, separation distance, and plume area. Standard-deviation images revealed areas of the plume characterized by intermittency; these regions were assumed to represent areas in which fuel and air had the potential for mixing. Time-averaged spontaneous vibrational Raman scattering provided quantitative assessments of the various plume properties. This technique offered direct measurements of the local equivalence ratio. Based on the equivalence-ratio maps and the published flammability limits of ethylene in air, the plume structure and mixing were documented in terms of flammable plume area and the required distance for the entire plume to reach flammable levels. A series of probe-based measurements were made and analyzed to determine the total pressure losses associated with each injection configuration.

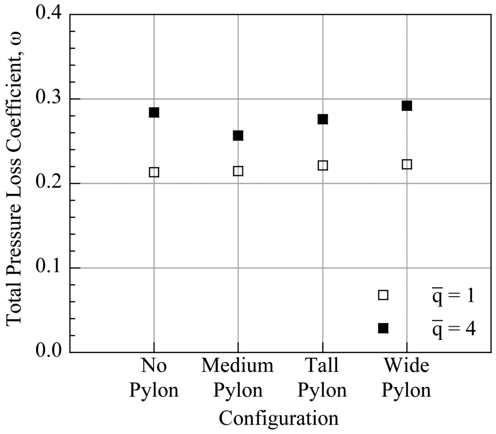

Fig. 20 Pressure loss coefficient for all configurations ($x/d = 12$).

The medium pylon provided the least enhancement in all aspects. It provided the lowest overall increase in penetration, compared with the reference case, and displayed similar plume area to the other pylons. Results indicated total pressure losses similar to those with the reference configuration. The tall pylon demonstrated interesting mixing and loss characteristics. It provided the highest plume penetration at the lowest jet-to-freestream momentum-flux ratio, but its fuel-plume-core location within the counter-rotating vortices prevented a sizeable increase in penetration at the higher injection conditions. The tall pylon did not significantly impact the total pressure loss. The wide pylon provided the best overall mixing performance of all the pylon configurations. Although similar to the tall- and medium-pylon configurations, it did provide slightly better values for penetration (based on the Raman-scattering results for high jet-to-freestream momentum-flux ratio), plume area, and flammable plume area. Additionally, the wide-pylon plume's trajectory characteristics were similar to those of the reference case. In general, the presence of the pylons increased the jet plume penetration and reduced the amount of injectant that remained near the wall, compared with a simple transverse injector. Mixing rate and pressure loss were not significantly influenced.

Some differences were observed between the NO-PLIF and Raman-scattering results. Specifically, the NO-PLIF results indicated that the tall pylon yielded the highest penetration at the highest jet-to-freestream momentum-flux ratio studied, and the Raman-scattering results indicated that the tall- and wide-pylon configurations had very similar levels of penetration at that condition. In addition, the plume-area analyses resulted in slight differences between the two sets of measurements. These differences illustrate the power of both diagnostic techniques: NO-PLIF resulted in rapid assessments of plume structure and the effects of the three pylons on the injection flowfield, whereas Raman scattering yielded quantitative mixing results that were used to better assess the evolution of the jet plume.

Acknowledgments

This work was supported by the U.S. Air Force Office of Scientific Research under the guidance of Julian Tishkoff. The support of the U.S. Air Force Research Laboratory, Propulsion Directorate, Research Air Facility is also appreciated. The authors would like to acknowledge the contributions of D. Schommer and W. Terry from Innovative Scientific Solutions, Inc., for their technical support of this work.

References

[1] Waitz, I. A., Marble, F. E., and Zukoski, E. E., "Investigation of a Contoured Wall Injector for Hypervelocity Mixing Augmentation," *AIAA Journal*, Vol. 31, No. 6, 1993, pp. 1014–1021.

[2] Hartfield, R. J., Hollo, S. D., and McDaniel, J. C., "Experimental Investigation of a Supersonic Swept Ramp Injector Using Laser-Induced Iodine Fluorescence," *Journal of Propulsion and Power*, Vol. 10, No. 1, 1994, pp. 129–135.

[3] Hollo, S. D., McDaniel, J. C., and Hartfield, R. J., "Quantitative Investigation of Compressible Mixing: Staged Transverse Injection into Mach 2 Flow," *AIAA Journal*, Vol. 32, No. 3, 1994, pp. 528–534.

[4] Barber, M. J., Roe, L. A., and Schetz, J. A., “Simulated Fuel Injection Through a Wedge-Shaped Orifice into Supersonic Flow,” AIAA Paper 95-2559, July 1995.

[5] Fuller, R. P., Wu, P. K., Nejad, A. S., and Schetz, J. A., “Comparison of Physical and Aerodynamic Ramps as Fuel Injectors in Supersonic Flow,” *Journal of Propulsion and Power*, Vol. 14, No. 2, 1998, pp. 135–145.

[6] Bonanos, A. M., Schetz, J. A., O’Brien, W. F., and Goyne, C. P., “Integrated Aeroramp-Injector/Plasma-Torch Igniter for Methane and Ethylene Fueled Scramjets,” AIAA Paper 2006-0813, Jan. 2006.

[7] Mathur, T., Cox-Stouffer, S., Hsu, K.-Y., Crafton, J., Donbar, J., and Gruber, M., “Experimental Assessment of a Fuel Injector for Scramjet Applications,” AIAA Paper 2000-3703, July 2000.

[8] Meicenheimer, H., Gutmark, E. J., Carter, C. D., Eklund, D. R., and Gruber, M. R., “A Computational Assessment of Independent Stage Control of a Cascade Injector,” AIAA Paper 2006-4863, July 2006.

[9] Srinivasan, R., and Bowersox, R. D. W., “Simulation of Transverse Gaseous Injection Through Diamond Ports into Supersonic Freestream,” *Journal of Propulsion and Power*, Vol. 23, No. 4, 2007, pp. 772–782.
doi:10.2514/1.18405

[10] Kobayashi, K., Bowersox, R. D. W., Srinivasan, R., Carter, C. D., and Hsu, K.-Y., “Flow Field Studies of Diamond Shaped Fuel Injector in a Supersonic Flow,” AIAA Paper 2007-5416, July 2007.

[11] Livingston, T., Segal, C., Schindler, M., and Vinogradov, V. A., “Penetration and Spreading of Liquid Jets in an External-Internal Compression Inlet,” *AIAA Journal*, Vol. 38, No. 6, 2000, pp. 989–994.

[12] Owens, M., Mullagiri, S., Segal, C., and Vinogradov, V., “Effects of Fuel Preinjection on Mixing in Mach 1.6 Airflow,” *Journal of Propulsion and Power*, Vol. 17, No. 3, 2001, pp. 605–610.

[13] Gouskov, O., Kopchenov, V., Lomkov, K. E., Vinogradov, V., and Waltrup, P. J., “Numerical Research of Gaseous Fuel Preinjection in Hypersonic Three-Dimensional Inlet,” *Journal of Propulsion and Power*, Vol. 17, No. 6, 2001, pp. 1162–1169.

[14] Vinogradov, V. A., Shikhman, Y., M., and Segal, C., “Review of Fuel Pre-Injection Studies in a High Speed Airflow,” AIAA Paper 2006-1030, Jan. 2006.

[15] Gilinsky, M., Khaikine, V., Akyurtlu, A., Akyurtlu, J., Trexler, C., Baurle, R., Emami, S., and Blankson, I. M., “Numerical and Experimental Tests of a Supersonic Inlet Utilizing a Pylon Set for Mixing, Combustion and Thrust Enhancement,” AIAA Paper 2005-0021, Jan. 2005.

[16] Gilinsky, M., Khaikine, V., Akyurtlu, A., Akyurtlu, J., Trexler, C., Baurle, R., Emami, S., and Blankson, I. M., “Numerical and Experimental Tests of a Supersonic Inlet Utilizing a Pylon Set for Mixing, Combustion and Thrust Enhancement,” AIAA Paper 2005-3290, May 2005.

[17] Akyurtlu, A., Akyurtlu, J., Gonor, A. L., Khaikine, V. A., Cutlet, A. D., and Blankson, I. M., “Numerical and Experimental Tests of a Supersonic Inlet with Pylon Set and Fuel Injection Through Pylons,” AIAA Paper 2006-1032, Jan. 2006.

[18] Montes, D. R., King, P. I., Gruber, M. R., Carter, C. D., and Hsu, K.-Y., “Mixing Effects of Pylon-Aided Fuel Injection Located Upstream of a Flameholding Cavity in Supersonic Flow,” AIAA Paper 2005-3913, July 2005.

[19] Haubelt, L. C., King, P. I., Gruber, M. R., Carter, C. D., and Hsu, K.-Y., “Performance of Pylons Upstream of a Cavity-Based Flameholder in Non-Reacting Supersonic Flow,” AIAA Paper 2006-4679, July 2006.

[20] Gruber, M. R., and Nejad, A. S., “New Supersonic Combustion Research Facility,” *Journal of Propulsion and Power*, Vol. 11, No. 5, 1995, pp. 1080–1083.

[21] Demtröder, W., *Laser Spectroscopy: Basic Concepts and Instrumentation*, Springer–Verlag, New York, 1981.

[22] Eckbreth, A. C., *Laser Diagnostics for Combustion Temperature and Species*, Abacus Press, Cambridge, MA, 1990.

[23] Haubelt, L. C., “Aerodynamic Loss and Mixing over a Cavity Flame Holder Located Downstream of Pylon-Aided Fuel Injection,” M.S. Thesis, Air Force Inst. of Technology, Wright–Patterson AFB, OH, 2006.

[24] Gruber, M. R., Nejad, A. S., Chen, T. H., and Dutton, J. C., “Compressibility Effects in Supersonic Transverse Injection Flowfields,” *Physics of Fluids*, Vol. 9, No. 5, 1997, pp. 1448–1461.
doi:10.1063/1.869257

[25] VanLerberghe, W. M., Dutton, J. C., Lucht, R. P., and Yuen, L. S., “Penetration and Mixing Studies of a Sonic Transverse Jet Injected into a Mach 1.6 Crossflow,” AIAA Paper 94-2246, June 1994.

[26] Montes, D. R., “Mixing Effects of Pylon-Aided Fuel Injection Located Upstream of a Flameholding Cavity in Supersonic Flow,” M.S. Thesis, Air Force Inst. of Technology, Wright–Patterson AFB, OH, 2005.

[27] Glassman, I., *Combustion*, Academic Press, New York, 1996.

[28] Schetz, J. A., Thomas, R. H., and Billig, F. S., “Mixing of Transverse Jets and Wall Jets in Supersonic Flow,” *Separated Flows and Jets*, Springer–Verlag, New York, 1990, pp. 807–837.

R. Bowersox
Associate Editor